



# Facile composition-controlled preparation and photocatalytic application of BiOCl/Bi<sub>2</sub>O<sub>2</sub>CO<sub>3</sub> nanosheets



Xiaochao Zhang<sup>a</sup>, Tianyu Guo<sup>b</sup>, Xiaowen Wang<sup>a</sup>, Yawen Wang<sup>a</sup>,  
Caimei Fan<sup>a,\*</sup>, Hui Zhang<sup>c</sup>

<sup>a</sup> College of Chemistry and Chemical Engineering, Taiyuan University of Technology, Taiyuan 030024, PR China

<sup>b</sup> Shanxi Province Industry and Trade College, Department of Chemical Engineering, Taiyuan 030024, PR China

<sup>c</sup> Particle Technology Research Centre, Department of Chemical and Biochemical Engineering, The University of Western Ontario, London, Ontario N6A 5B9, Canada

## ARTICLE INFO

### Article history:

Received 23 September 2013

Received in revised form

25 December 2013

Accepted 30 December 2013

Available online 7 January 2014

### Keywords:

Composition-controlled synthesis

BiOCl/Bi<sub>2</sub>O<sub>2</sub>CO<sub>3</sub>

Photocatalytic activity

Electron-hole separation

First-principles calculation

## ABSTRACT

The BiOCl, BiOCl/Bi<sub>2</sub>O<sub>2</sub>CO<sub>3</sub> composites and Bi<sub>2</sub>O<sub>2</sub>CO<sub>3</sub> were successfully fabricated by a facile composition-controlled preparation technology at room temperature for the first time. The X-ray diffraction (XRD), scanning electron microscopy (SEM), Brunauer–Emmett–Teller (BET) adsorption isotherm, UV–vis diffuse reflectance spectra (UV–vis DRS) and first-principles methods were employed to characterize the phase structures, morphologies, surface areas, optical properties, and photocatalytic mechanism of as-prepared samples. The BiOCl/Bi<sub>2</sub>O<sub>2</sub>CO<sub>3</sub> composites exhibited the higher photocatalytic activity than individual BiOCl and Bi<sub>2</sub>O<sub>2</sub>CO<sub>3</sub> for the degradation of MO under simulated sunlight irradiation. The COD removal efficiency of MO solution over BiOCl/Bi<sub>2</sub>O<sub>2</sub>CO<sub>3</sub> composite achieved 95% after 8 h reaction time. In addition, the formation mechanism and excellent photocatalytic activity of BiOCl/Bi<sub>2</sub>O<sub>2</sub>CO<sub>3</sub> composite have been investigated and discussed in detail. The enhanced photocatalytic performance of BiOCl/Bi<sub>2</sub>O<sub>2</sub>CO<sub>3</sub> composites is closely related to the suitable conduction band (CB) interaction and efficient separation of photo-induced electron-hole pairs by the synergistic effect of BiOCl and Bi<sub>2</sub>O<sub>2</sub>CO<sub>3</sub> under the simulated sunlight irradiation. Combined with the theoretical and experimental findings, the photocatalytic mechanism of BiOCl/Bi<sub>2</sub>O<sub>2</sub>CO<sub>3</sub> composite and the charge carrier transfer process between Bi<sub>2</sub>O<sub>2</sub>CO<sub>3</sub> and BiOCl semiconductors have been proposed and investigated.

© 2014 Elsevier B.V. All rights reserved.

## 1. Introduction

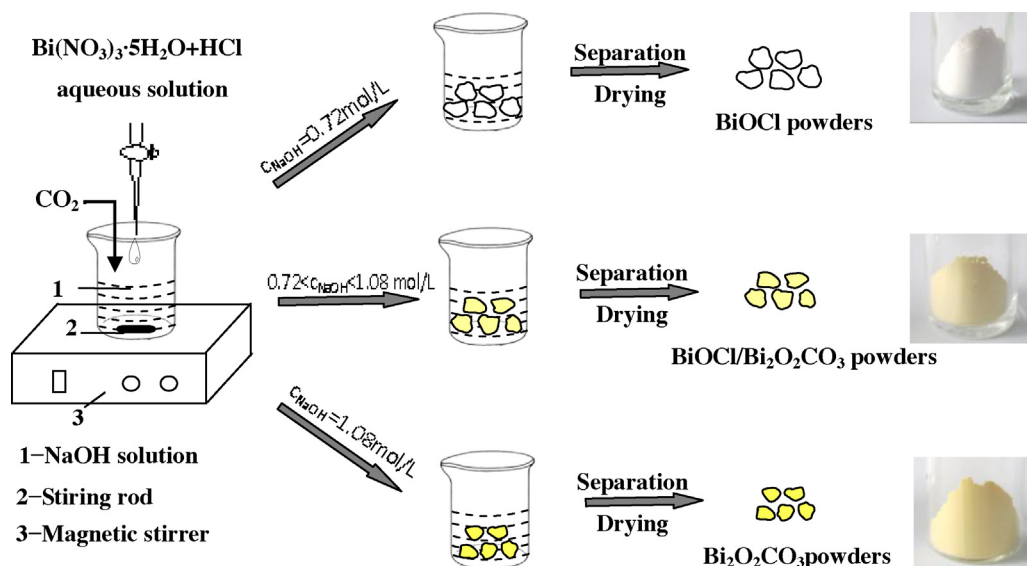
In the past decades, photocatalysis technology, which has been highly expected to be an ideal “green” technology by the utilization of solar energy [1], has been widely applied in several fields, such as, solar cell [2], water-splitting [3], organic pollutant degradation [4], CO<sub>2</sub> reduction [5], and so on. Most recently, bismuth compounds have drawn considerable attention for the promising practical industrial application in the photocatalytic materials [6–8]. For instance, Zhang et al. [6] firstly reported that BiOCl semiconductor exhibited better photocatalytic activity than P25 at three-cycles for decomposing methyl orange (MO) dye under ultraviolet (UV) light irradiation. Since then, BiOCl, as a novel photocatalyst, has attracted tremendous interests in the photocatalysis field owing to its particular layer structure, electronic property, outstanding photocatalytic activity and stability [9–11]. Most importantly, BiOCl semiconductor with an indirect transition band gap makes the

photoexcited electrons emitted to the valence band by a certain *k*-space distance, reducing the recombination probability of photo-excited electrons and holes [12]. However, the potential for wonderful photocatalytic application is seriously confined due to the wider band gap of 3.05 ~ 3.55 eV [8–12] for pure BiOCl, so it can only absorb the ultraviolet (UV) light (about 4% of solar energy) to activate its useful functionality by photo-induced charge carriers.

Semiconductor combination that constructs a heterojunction interface between two types of semiconductors with matching energy band gaps, has been extensively adopted to enhance the efficient separation of photo-generated charge carriers and realize the overall response of solar spectra, and consequently, achieving the higher efficiency for the decomposition of organic compounds in wastewater or air. Previously, many BiOCl composite systems, such as BiOCl/Bi<sub>2</sub>O<sub>3</sub> [13], BiOCl/WO<sub>3</sub> [14], BiOCl/NaBiO<sub>3</sub> [15], BiOCl/ZnO [16], BiOCl/Bi<sub>2</sub>S<sub>3</sub> [17], BiOCl/Ag<sub>3</sub>PO<sub>4</sub> [18], and so on, have been reported, which exhibited relatively higher photocatalytic activity and stability under visible light or solar light irradiation, especially, the Bi-based composite BiOCl systems. For example, the BiOCl/Bi<sub>2</sub>O<sub>3</sub> heterojunction composite could provide unexpectedly higher photocatalytic performance than individual BiOCl and Bi<sub>2</sub>O<sub>3</sub>

\* Corresponding author. Tel.: +86 13007011210; fax: +86 351 6018554.

E-mail addresses: [fanm@163.com](mailto:fanm@163.com), [zhang13598124761@163.com](mailto:zhang13598124761@163.com) (C. Fan).



**Scheme 1.** Schematic illustration for the proposed formation process of samples by a facile method with controlling the concentration of NaOH.

photocatalyst in decomposing organic compounds under visible light irradiation [13]. Most interestingly, in the formation process of  $\text{Bi}_2\text{O}_3$ , a novel  $\text{Bi}_2\text{O}_2\text{CO}_3$  semiconductor is usually formed as intermediated product [19–21]. As Bi-based nanostructured material with particular layered structures,  $\text{Bi}_2\text{O}_2\text{CO}_3$  that constitutes of layered structure with alternative stacking of  $(\text{Bi}_2\text{O}_2)^{2+}$  sheets interleaved by  $\text{CO}_3^{2-}$  groups reveals unique photocatalytic properties under UV–vis light irradiation [22,23]. Therefore,  $\text{Bi}_2\text{O}_2\text{CO}_3$  has also been received widespread attention for the potential application in the photocatalysis field in recent years [24–28]. For instance, Zheng et al. [24] reported firstly that the  $\text{Bi}_2\text{O}_2\text{CO}_3$  photocatalyst had the good photodegradation of Rhodamine-B (RhB) under UV light irradiation. Zhao et al. [25] successfully synthesized sponge-, rose- and plate-like  $\text{Bi}_2\text{O}_2\text{CO}_3$  structure at  $180^\circ\text{C}$  in a span of 24 h using tri-sodium citrate as the coordinating agent and carbon source through a hydrothermal process, and the sponge-like  $\text{Bi}_2\text{O}_2\text{CO}_3$  sample exhibited excellent visible-light-photocatalytic activity for the degradation of dyes under 300 W Xe-lamp light irradiation. In addition,  $\text{Bi}_2\text{O}_2\text{CO}_3$  nanosheet with a thickness of less than 20 nm was synthesized via hydrothermal and solvothermal process by Huang et al. [26,27]. However, it is found that the previous synthesis processes of  $\text{Bi}_2\text{O}_2\text{CO}_3$  with well-defined nanostructures or all-right photocatalytic activity could be done under severe conditions of longer reaction time and/or higher temperature, thus it is attractive to develop a facile, simple and convenient method for the synthesis of  $\text{Bi}_2\text{O}_2\text{CO}_3$  with higher photocatalytic activity and stability.

Wondrously and delightedly, in the synthesis processes of BiOCl using a facile method, it is found that BiOCl, BiOCl/ $\text{Bi}_2\text{O}_2\text{CO}_3$  composites and  $\text{Bi}_2\text{O}_2\text{CO}_3$  may be successfully prepared by controlling the concentration of NaOH under the same conditions in our lab. Meanwhile, the photocatalytic activities of BiOCl/ $\text{Bi}_2\text{O}_2\text{CO}_3$  composites are obviously higher than individual BiOCl and  $\text{Bi}_2\text{O}_3\text{CO}_3$  under simulated sunlight irradiation. The attracted experimental phenomena and results arouse our great interests, and it is expected to provide the significant achievements to develop the practical application for such similar particular Bi-based photocatalytic materials. In the present work, BiOCl, BiOCl/ $\text{Bi}_2\text{O}_2\text{CO}_3$  composites and  $\text{Bi}_2\text{O}_2\text{CO}_3$  were firstly fabricated at room temperature by a facile method with controlling the different concentration of NaOH. The as-synthesized samples were characterized by XRD, SEM, BET, and UV–vis DRS. The photocatalytic activities were evaluated by

the photocatalytic degradation of MO under simulated sunlight irradiation. Finally, the photocatalytic mechanism and effective separation of photo-induced electron-hole for BiOCl/ $\text{Bi}_2\text{O}_2\text{CO}_3$  composite have been investigated and discussed in detail on the basis of the experimental and computational methods.

## 2. Experiments

### 2.1. Catalyst preparation

All the reagents are of analytic grade and used without further purification. 1.940 g  $\text{Bi}(\text{NO}_3)_3 \cdot 5\text{H}_2\text{O}$  was dissolved in 20 ml HCl of 1.5 mol/L to get a transparent solution (named as solution A). Then, the solution A was added dropwise into a certain concentration of NaOH solution with constant stirring rate, and there exist several precipitations in the mixed solution. After titration, the mixture solution was stirred for 10 min and then the precipitates were filtrated and washed for several times with distilled water, followed by drying at  $80^\circ\text{C}$  for 4 h.

Scheme 1 shows the schematic illustration for the proposed formation process of samples by a facile method with controlling the concentration of NaOH solution. When the solution A composed of HCl and  $\text{Bi}(\text{NO}_3)_3 \cdot 5\text{H}_2\text{O}$  was dripped into the various concentration of NaOH solution, interestingly obtaining the different color precipitates. In consideration of the attracted experimental phenomena, a series of tests have been carried out in our lab. The experimental results indicated that the white precipitates which have been proved to be pure BiOCl samples could be generated at the NaOH concentration of 0.72 mol/L. The yellow precipitates (pure  $\text{Bi}_2\text{O}_2\text{CO}_3$  samples) could be obtained at the NaOH concentration of 1.08 mol/L; there are pale yellow BiOCl/ $\text{Bi}_2\text{O}_2\text{CO}_3$  composites (named as BiOCl/ $\text{CO}_3$ -1, BiOCl/ $\text{CO}_3$ -2 and BiOCl/ $\text{CO}_3$ -3) at the NaOH concentration of 0.81, 0.90 and 0.99 mol/L, as testified in Fig. 1.

### 2.2. Characterizations

The crystalline structures of as-prepared products were analyzed using an X-ray diffractometer (XRD) with a D/max-2500 diffractometer ( $\text{CuK}\alpha$ ,  $\lambda = 1.5406 \text{ \AA}$ ) at the scanning range of  $10$ – $70^\circ$ . The morphology of as-prepared samples was examined using a Nanosem430 field emission scanning electron microscope equipped with an energy-dispersive spectroscopic (EDS) device.

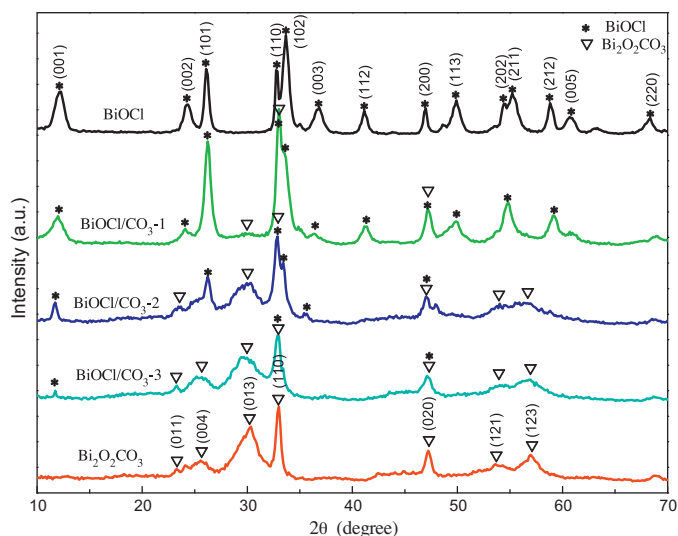


**Fig. 1.** XRD patterns of as-synthesized BiOCl, BiOCl/CO<sub>3</sub>-1, BiOCl/CO<sub>3</sub>-2, BiOCl/CO<sub>3</sub>-3, Bi<sub>2</sub>O<sub>2</sub>CO<sub>3</sub> samples.

UV–vis diffused reflectance spectra of samples were obtained for the dry-pressed film samples using UV–vis spectrophotometer (UV-3600, Shimadzu, Japan). BaSO<sub>4</sub> was used as a reflectance standard in the UV–vis diffuse reflectance experiment. The N<sub>2</sub> adsorption–desorption analysis was measured on a NOVA 4000 (Quantachrome Corporation) instrument.

### 2.3. Photocatalytic activity

The photocatalytic properties of pure BiOCl, BiOCl/Bi<sub>2</sub>O<sub>2</sub>CO<sub>3</sub> composites and pure Bi<sub>2</sub>O<sub>2</sub>CO<sub>3</sub> samples were evaluated by the degradation of methyl orange (MO) at ambient temperature using a 500 W Xe-lamp with a refrigerating water circuit as a slide light source. Typically, 0.05 g photocatalyst was added into 50 mL of 10 mg L<sup>-1</sup> MO aqueous solution in a container. During the degradation process, the MO solution with photocatalyst was aerated by air through a mini-type pump to keep catalyst uniform distribution in the solution. At given time intervals, the residual MO in the solution was determined over a varian Cary-50 UV–vis spectrophotometer.

### 2.4. First-principles calculation

In this study work, first-principles calculation has been performed using the well-tested Cambridge Serial Total Energy Package (CASTEP) code based on density functional theory (DFT) [28]. The exchange–correlation functional was described with the generalized gradient approximation (GGA) within the scheme of Perdew–Burke–Ernzerhof (PBE) [29]. For relative investigations on the electronic structures and ground-state properties of BiOCl and Bi<sub>2</sub>O<sub>2</sub>CO<sub>3</sub>, the valence electronic configurations are Bi-6s<sup>2</sup>6p<sup>3</sup>, O-2s<sup>2</sup>2p<sup>4</sup>, Cl-3s<sup>2</sup>3p<sup>5</sup>, and C-2s<sup>2</sup>2p<sup>2</sup> states. The cutoff energy of 380 eV is applied in the Kohn–Sham wave function of valence electrons, and the Brillouin zone integrations were approximated using a 3 × 3 × 3 *k*-point grid sampling scheme of Monkhorst–Pack [30].

In order to further obtain reasonable results, the lattice parameters of BiOCl and Bi<sub>2</sub>O<sub>2</sub>CO<sub>3</sub> crystals were optimized by an iterative process, in which the maximum root-mean-square convergent tolerance, force convergence thresholds, and stress tolerances are less than 1 × 10<sup>-6</sup> eV/atom, 0.1 eV/nm, and 0.05 GPa, respectively. Then, the electronic band structures of the optimized BiOCl and Bi<sub>2</sub>O<sub>2</sub>CO<sub>3</sub> were calculated and further discussed in detail.

## 3. Results and discussion

### 3.1. XRD analyses of samples

The phase structure characterization has been investigated by means of X-ray powder diffraction (XRD), and the typical diffraction patterns of as-prepared samples have been shown in Fig. 1. All the diffraction peaks of BiOCl can be readily indexed to the standard diffraction data of tetragonal BiOCl (JCPDS card No. 06-0249, lattice constants *a* = *b* = 3.891 Å and *c* = 7.369 Å), and no other impurity phases were detected, indicating that pure tetragonal BiOCl phase has been obtained. What's more, the intense diffraction peaks of tetragonal BiOCl suggest that as-synthesized sample should be well crystallized. However, the diffraction peaks of Bi<sub>2</sub>O<sub>2</sub>CO<sub>3</sub> are relatively broadened because an occurred lattice distortion usually caused the lowering of crystallinity, and microstrain effects that may provide more point defects such as oxygen vacancy [25,31]. Such similar diffraction peak characterizations of tetragonal Bi<sub>2</sub>O<sub>2</sub>CO<sub>3</sub> had been previously reported in the synthetic experiments of Bi<sub>2</sub>O<sub>2</sub>CO<sub>3</sub> nanostructures photocatalyst by Dong et al. [20], Xie et al. [24], and Zhao et al. [25], which could be indexed to tetragonal Bi<sub>2</sub>O<sub>2</sub>CO<sub>3</sub> (JCPDS card No. 41-1488, lattice constants *a* = *b* = 3.865 Å and *c* = 13.67 Å). The low intensity and broad width of the diffraction peaks for as-prepared Bi<sub>2</sub>O<sub>2</sub>CO<sub>3</sub> sample could be correlated with this synthesis technology with controlling the NaOH concentration, resulting in an unavoidable lattice distortion due to the transformation from tetragonal BiOCl to Bi<sub>2</sub>O<sub>2</sub>CO<sub>3</sub> in the synthesis process. Although the as-prepared Bi<sub>2</sub>O<sub>2</sub>CO<sub>3</sub> has a poor crystallinity, the significant XRD diffraction peaks of (0 1 3), (1 1 0), (0 2 0), and (1 2 3) for tetragonal Bi<sub>2</sub>O<sub>2</sub>CO<sub>3</sub> remain to be obvious. In addition, it is remarkable to mention that the intensity ratio of (1 1 0)–(0 1 3) peaks of Bi<sub>2</sub>O<sub>2</sub>CO<sub>3</sub> is 1.298, much higher than the standard value (0.386) and other reported data of 0.582 [24] and 0.587 [26,32], which indicates that the preferred anisotropic growth of as-prepared Bi<sub>2</sub>O<sub>2</sub>CO<sub>3</sub> is along the (1 1 0) plane.

For the XRD patterns of as-prepared BiOCl/CO<sub>3</sub>-1, BiOCl/CO<sub>3</sub>-2, BiOCl/CO<sub>3</sub>-3 composites, with the increasing NaOH concentration, a few diffraction peaks of tetragonal BiOCl gradually shift and transfer into ones of Bi<sub>2</sub>O<sub>2</sub>CO<sub>3</sub>, obtaining a small part of tetragonal Bi<sub>2</sub>O<sub>2</sub>CO<sub>3</sub> components, which is inconspicuous due to the same phase structure with the partially similar diffraction peaks between BiOCl and Bi<sub>2</sub>O<sub>2</sub>CO<sub>3</sub>. The percentages of BiOCl and Bi<sub>2</sub>O<sub>2</sub>CO<sub>3</sub> components in BiOCl/Bi<sub>2</sub>O<sub>2</sub>CO<sub>3</sub> composites have been calculated through Jade 5.0, as shown in Table 1. The calculated data show that, with the increase of NaOH concentration, the percentage of obtained BiOCl component decreases, while one of Bi<sub>2</sub>O<sub>2</sub>CO<sub>3</sub> component gradually increases. Besides, the color change of as-prepared samples in our experiment phenomena, as displayed in

**Table 1**  
Amount percentages, sizes, surface areas, and reaction rates of as-prepared samples.

	BiOCl	BiOCl/CO <sub>3</sub> -1	BiOCl/CO <sub>3</sub> -2	BiOCl/CO <sub>3</sub> -3	Bi <sub>2</sub> O <sub>2</sub> CO <sub>3</sub>
Amount of Bi <sub>2</sub> O <sub>2</sub> CO <sub>3</sub> (%)	0	12.92	36.10	65.42	100
Amount of BiOCl (%)	100	87.08	63.90	34.58	0
Size (nm)	12.8	11.7	18.0	11.3	9.7
<i>k</i> (min <sup>-1</sup> )	0.004	0.014	0.027	0.017	0.011
<i>S</i> <sub>BET</sub> (m <sup>2</sup> g <sup>-1</sup> )	19.07	37.73	33.43	43.73	20.60

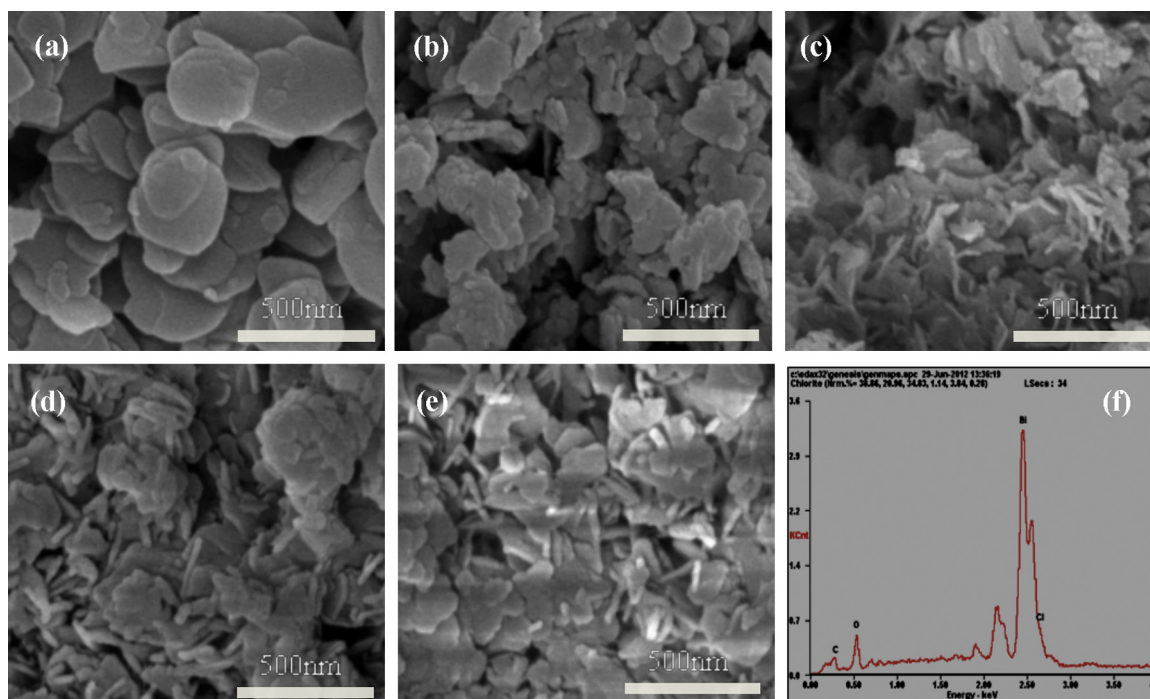


Fig. 2. SEM images of as-synthesized samples (a) BiOCl, (b) BiOCl/CO<sub>3</sub>-1, (c) BiOCl/CO<sub>3</sub>-2, (d) BiOCl/CO<sub>3</sub>-3, (e) Bi<sub>2</sub>O<sub>2</sub>CO<sub>3</sub>, and (f) EDS spectrum of BiOCl/CO<sub>3</sub>-2.

Fig. 1, could be attributed to the change of component. From XRD patterns of BiOCl/Bi<sub>2</sub>O<sub>2</sub>CO<sub>3</sub> composites, it can be clearly seen that the typical (0 1 3) and (1 1 0) peaks (at 30.25° and 32.73°) intensity of Bi<sub>2</sub>O<sub>2</sub>CO<sub>3</sub> increases obviously, and the (0 0 1), (1 0 1), (1 0 2) characteristic peaks (at 11.98°, 25.86°, and 33.45°) intensity of BiOCl gradually decreases from BiOCl/CO<sub>3</sub>-1 to BiOCl/CO<sub>3</sub>-3 samples. The results reveal that BiOCl, BiOCl/Bi<sub>2</sub>O<sub>2</sub>CO<sub>3</sub> composites and Bi<sub>2</sub>O<sub>2</sub>CO<sub>3</sub> could be obtained by a facile composition-controlled preparation technology with controlling the concentration of NaOH solution at room temperature.

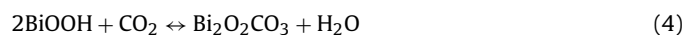
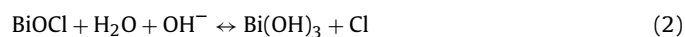
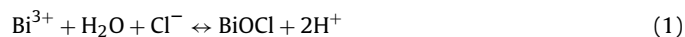
In addition, the average grain sizes of as-prepared products have been calculated according to the Scherrer formula, and the specific surface areas of samples were measured by N<sub>2</sub> adsorption–desorption analysis, as shown in Table 1. The obtained specific surface areas of BiOCl and Bi<sub>2</sub>O<sub>2</sub>CO<sub>3</sub> are 19.07 and 20.60 m<sup>2</sup>/g, respectively, smaller than BiOCl/CO<sub>3</sub>-1, BiOCl/CO<sub>3</sub>-2, and BiOCl/CO<sub>3</sub>-3 composites of 37.73, 33.43, and 43.73 m<sup>2</sup>/g. The average grain sizes are between 9.7 and 18.0.

### 3.2. Morphology and formation mechanism of samples

The scanning electronic microscopy (SEM) images of the as-prepared products are shown in Fig. 2(a–e). According to the SEM characterization observations, with the increasing NaOH concentration, the morphologies of as-prepared samples are all irregular like-sheets structure, and the nanosheets exhibit the different arrangement and structure behaviors. As shown in Fig. 2(a), the thickness and length of BiOCl nanosheets are about 20 nm and 300 nm. BiOCl/CO<sub>3</sub>-1 nanosheets (Fig. 2(b)) displays an agglomeration to certain extent owing to the appearance of Bi<sub>2</sub>O<sub>2</sub>CO<sub>3</sub> with the increase of NaOH concentration, and keep the original growth direction of BiOCl nanosheets, which may be ascribed to the existence of a formed small amount of Bi<sub>2</sub>O<sub>2</sub>CO<sub>3</sub> which will adhere to the BiOCl nanosheets surface. However, on the basis of the appropriate Bi<sub>2</sub>O<sub>2</sub>CO<sub>3</sub> amounts, BiOCl/CO<sub>3</sub>-2 nanosheets (Fig. 2(c)) intersect with each other along the different directions and stack randomly, so that the special morphology of BiOCl/CO<sub>3</sub>-2 composite possesses the appropriate specific surface area, and

the thickness of nanosheets becomes obviously thin compared with other samples, which could facilitate the multiple scattering of UV–vis light, resulting in the greater light-harvesting capacity [24]. In Fig. 2(d), the morphology characterization of BiOCl/CO<sub>3</sub>-3 nanosheets is similar to BiOCl/CO<sub>3</sub>-1 composite, but there is the noteworthy bar-shaped analogs adhering to the nanosheet edges for BiOCl/CO<sub>3</sub>-3, which may be derived from the existence of a large number of crystallized Bi<sub>2</sub>O<sub>2</sub>CO<sub>3</sub> in the preparation of transitioning from tetragonal BiOCl to Bi<sub>2</sub>O<sub>2</sub>CO<sub>3</sub> crystals, displayed in Fig. 1. As is well known, the lattice constant  $c = 13.67 \text{ \AA}$  of tetragonal Bi<sub>2</sub>O<sub>2</sub>CO<sub>3</sub> is much larger than  $c = 7.369 \text{ \AA}$  of tetragonal BiOCl, and  $a = b$  of Bi<sub>2</sub>O<sub>2</sub>CO<sub>3</sub> is slightly less than BiOCl, such that the lattice distortion (especially  $c$ -direction) could happen in the crystal transition process. After the formation of pure Bi<sub>2</sub>O<sub>2</sub>CO<sub>3</sub>, the length of nanosheets is obvious smaller than pure BiOCl, and there is rather similar thickness. In addition, the constituents of BiOCl/CO<sub>3</sub>-2 have been studied using EDS spectrum method, as shown in Fig. 2(f). The analysis results indicate the sole presence of Bi, O, Cl, and C atoms, demonstrating the coexistence of BiOCl and Bi<sub>2</sub>O<sub>2</sub>CO<sub>3</sub> in the BiOCl/CO<sub>3</sub>-2 sample.

One the basis of the above analysis, the probable pathways during the formation processes of the expected products in our experiments can be summarized in Eqs. (1)–(4) as follows.



At the initial stage of the reaction, since the Bi(NO<sub>3</sub>)<sub>3</sub>·5H<sub>2</sub>O and HCl aqueous solution with Bi<sup>3+</sup> and Cl<sup>−</sup> ions was dropped into NaOH aqueous solution, Bi<sup>3+</sup> ions were subjected to a complete hydrolysis and react with Cl<sup>−</sup> and H<sub>2</sub>O, obtaining pure BiOCl (pH 2, seen in Eq. (1)). With the increase of OH<sup>−</sup> concentration, the produced BiOCl further made a performance to react with suitable



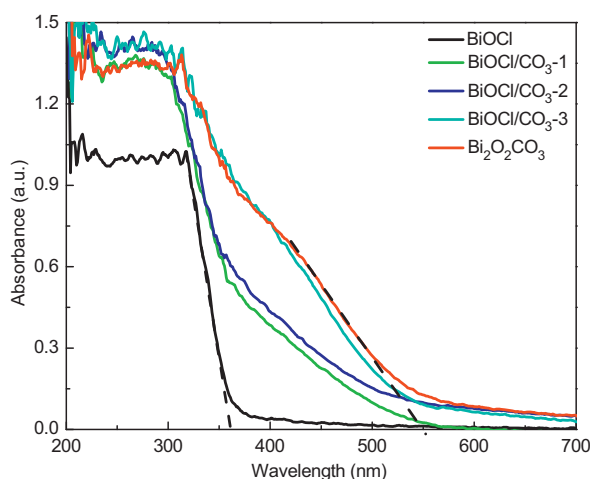


**Fig. 3.** UV-vis diffuse reflectance spectra of BiOCl, BiOCl/Bi<sub>2</sub>O<sub>2</sub>CO<sub>3</sub>, and Bi<sub>2</sub>O<sub>2</sub>CO<sub>3</sub> samples.

OH<sup>−</sup> ions, obtaining the intermediate product of Bi(OH)<sub>3</sub>, seen in Eq. (2) [33,34]. The rather unstable Bi(OH)<sub>3</sub> is very easy to be decomposed into BiOOH and H<sub>2</sub>O under the stirring condition (Eq. (3)), followed by the occurrence of reaction with CO<sub>2</sub> originated from air to form Bi<sub>2</sub>O<sub>2</sub>CO<sub>3</sub>, and consequently, BiOCl crystal will transform to Bi<sub>2</sub>O<sub>2</sub>CO<sub>3</sub> crystal, seen in Eq. (4). Herein, in order to clarify the synthesis reproducibility of our samples, we have again synthesized the BiOCl/CO<sub>3</sub>-2 composite according to the same condition and process in the present work, and the XRD patterns of reproducible samples are the same as ones of our previous samples, (please see in Supplementary Fig. S1). The results indicate that the variety of products can be obtained and controlled by the value of *C*<sub>NaOH</sub> with the existence of appropriate CO<sub>2</sub> concentration from air in the lab, thus the preparation method is simple, reliable and has good repeatability.

### 3.3. UV-vis diffuse reflectance spectra

The optical absorption properties of semiconductor materials are closely relevant to their electronic band structures and recognized as important factors to evaluate their photocatalytic activity. Fig. 3 shows the UV-vis diffuse reflectance spectra of as-prepared BiOCl, BiOCl/CO<sub>3</sub>-1, BiOCl/CO<sub>3</sub>-2, BiOCl/CO<sub>3</sub>-3, and Bi<sub>2</sub>O<sub>2</sub>CO<sub>3</sub> samples. It can be seen that, pure BiOCl has an absorption edge at about 365 nm and pure Bi<sub>2</sub>O<sub>2</sub>CO<sub>3</sub> exhibits a strong optical adsorption in the UV-vis region from 200 to 500 nm. The absorption edge at 550 nm of pure Bi<sub>2</sub>O<sub>2</sub>CO<sub>3</sub> indicates that the visible-light absorption is attributed to the intrinsic band-gap transition. Compared with pure BiOCl, the observed red shifts of BiOCl/Bi<sub>2</sub>O<sub>2</sub>CO<sub>3</sub> composites may be attributed to the existence of Bi<sub>2</sub>O<sub>2</sub>CO<sub>3</sub> crystal, resulting in a possible charge-transfer transition on the interface between BiOCl and Bi<sub>2</sub>O<sub>2</sub>CO<sub>3</sub>, and consequently, enhancing the optical absorption intensity and extending gradually the optical absorption edges of BiOCl/Bi<sub>2</sub>O<sub>2</sub>CO<sub>3</sub> with the increasing Bi<sub>2</sub>O<sub>2</sub>CO<sub>3</sub> component.

For a crystalline semiconductor, the optical absorption near band edge follows the formula  $(\alpha h\nu)^n = A(h\nu - E_g)$  [24], where  $\alpha$ ,  $h$ ,  $\nu$ ,  $E_g$ , and  $A$  represent the absorption coefficient, Planck constant, light frequency, band gap, and proportionality constant, respectively. The  $n$  values are 2 and 1/2 for direct and indirect inter-band transition semiconductors. In this work, the calculated band gaps of pure BiOCl and Bi<sub>2</sub>O<sub>2</sub>CO<sub>3</sub> exhibit the indirect and direct inter-band transition characteristic, respectively, as seen in Fig. 4, so the experimental optical band gaps of BiOCl and Bi<sub>2</sub>O<sub>2</sub>CO<sub>3</sub> are determined from the plot  $(\alpha h\nu)^{1/2}$  against  $(h\nu)$  and plot  $(\alpha h\nu)^2$  against  $(h\nu)$ , estimated to be about 3.40 eV and 2.23 eV, respectively. In

addition, the conduction band (CB) and valence band (VB) potentials of pure BiOCl and Bi<sub>2</sub>O<sub>2</sub>CO<sub>3</sub> crystal at the point of zero charge could be calculated by Butler and Ginley using the following formula [35]:

$$E_{VB} = X - E^e + 0.5E_g \quad (5)$$

$$E_{CB} = E_{VB} - E_g \quad (6)$$

where  $X$  is the absolute electronegativity of semiconductor material involving the geometric mean of the electronegativities of constituent atoms;  $E^e$  is the energy of free electrons on the hydrogen scale (ca. 4.5 eV);  $E_{VB}$  and  $E_g$  are the VB edge potential and band gap of semiconductor, respectively. The  $X$  values for BiOCl and Bi<sub>2</sub>O<sub>2</sub>CO<sub>3</sub> were determined to be 6.36 eV. On the basis of the above following formula, the valence band maximum (VBM) and conduction band minimum (CBM) of pure BiOCl and Bi<sub>2</sub>O<sub>2</sub>CO<sub>3</sub> are calculated to be 3.56 and 0.16 eV, 2.98 and 0.75 eV, respectively.

Moreover, the electronic energy band structures and total densities of states (TDOS) of BiOCl and Bi<sub>2</sub>O<sub>2</sub>CO<sub>3</sub> crystals are further investigated using first-principles method based on density functional theory (DFT), as shown in Fig. 4. From Fig. 4(a), it can be found that tetragonal BiOCl crystal belongs to indirect gap semiconductor material, and the minimum indirect gap is 2.64 eV from the valence band maximum (VBM) between F and G points to the conduction band minimum (CBM) at the G point of 2.64 eV, coincident with the previously reported results of 2.64 eV [36] by Huang et al. and 2.64 eV [37] by Fan et al. However, tetragonal Bi<sub>2</sub>O<sub>2</sub>CO<sub>3</sub> crystal is a direct gap semiconductor material, and its band gap value is 1.21 eV originating from the electronic transition from 0 eV to 1.21 eV at the same G point, as shown in Fig. 4(b). The theoretical band gap values are less than our experimental data, which agrees with the general rule that the self-consistent DFT calculation usually underestimates the band gaps of semiconductor materials [28].

To understand the electronic state composition of CB and VB, the partial density of states (PDOS) for tetragonal BiOCl and Bi<sub>2</sub>O<sub>2</sub>CO<sub>3</sub> crystals are plotted in Fig. 5. As shown in Fig. 5(a), the VBM of tetragonal BiOCl crystal is mainly contributed by the hybridization of the occupied O 2p and Cl 3p states with a small part of Bi 6s states, and the CBM by the unoccupied Bi 6p states, resulting in that an indirect electronic transition from occupied O 2p and Cl 3p states in VBM to unoccupied Bi 6p states in CBM. We can see from Fig. 5(b) that the CBM and VBM of tetragonal Bi<sub>2</sub>O<sub>2</sub>CO<sub>3</sub> crystal are mainly dominated by unoccupied Bi 6p states and occupied O 2p states derived from O atoms of CO<sub>3</sub><sup>2−</sup> slab, respectively, which will facilitate the effective electronic transition between Bi<sub>2</sub>O<sub>2</sub><sup>2+</sup> layer and CO<sub>3</sub><sup>2−</sup> slab.

### 3.4. Photocatalytic activity

The as-prepared BiOCl, BiOCl/CO<sub>3</sub>-1, BiOCl/CO<sub>3</sub>-2, BiOCl/CO<sub>3</sub>-3, and Bi<sub>2</sub>O<sub>2</sub>CO<sub>3</sub> were evaluated by the photocatalytic removal of MO solution as a function of irradiation time under simulated sunlight irradiation, shown in Fig. 6(a). The results reveal that BiOCl/Bi<sub>2</sub>O<sub>2</sub>CO<sub>3</sub> composites display much better photocatalytic activity than individual BiOCl and Bi<sub>2</sub>O<sub>2</sub>CO<sub>3</sub> photocatalyst under simulated sunlight irradiation, and the MO degradation efficiencies of BiOCl/CO<sub>3</sub>-1, BiOCl/CO<sub>3</sub>-2, and BiOCl/CO<sub>3</sub>-3 composites are 90%, 99%, and 95% after 150 min, respectively, obviously higher than 46% and 81% of BiOCl and Bi<sub>2</sub>O<sub>2</sub>CO<sub>3</sub>. In addition, Fig. 6(b) displays the linear relationship between  $\ln(C_0/C)$  and irradiation time, suggesting that the photocatalytic degradation reaction of MO over the as-prepared catalysts should belong to the first-order kinetic relation. The calculated reaction rates have been shown in Table 1. The reaction rate constant of 0.027 min<sup>−1</sup> for BiOCl/CO<sub>3</sub>-2 is as 2.5 and 7 times as ones for Bi<sub>2</sub>O<sub>2</sub>CO<sub>3</sub> and BiOCl. The enhanced photocatalytic activity of BiOCl/Bi<sub>2</sub>O<sub>2</sub>CO<sub>3</sub> may be associated with the heterojunction effect of BiOCl and Bi<sub>2</sub>O<sub>2</sub>CO<sub>3</sub>.

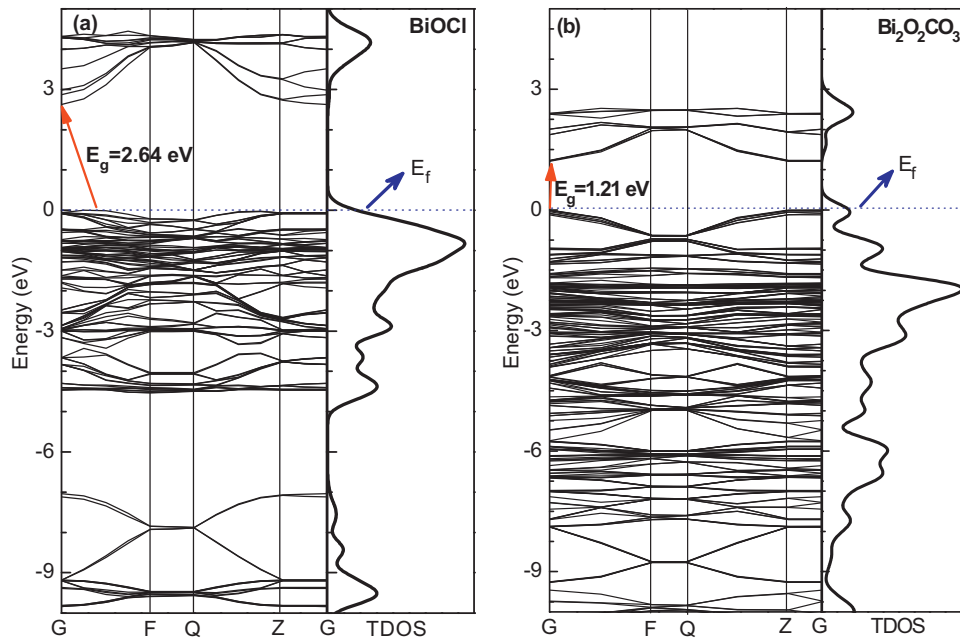


**Fig. 4.** Electronic energy band structures and total densities of states (TDOS) of tetragonal BiOCl and  $\text{Bi}_2\text{O}_2\text{CO}_3$  crystals using first-principles method.

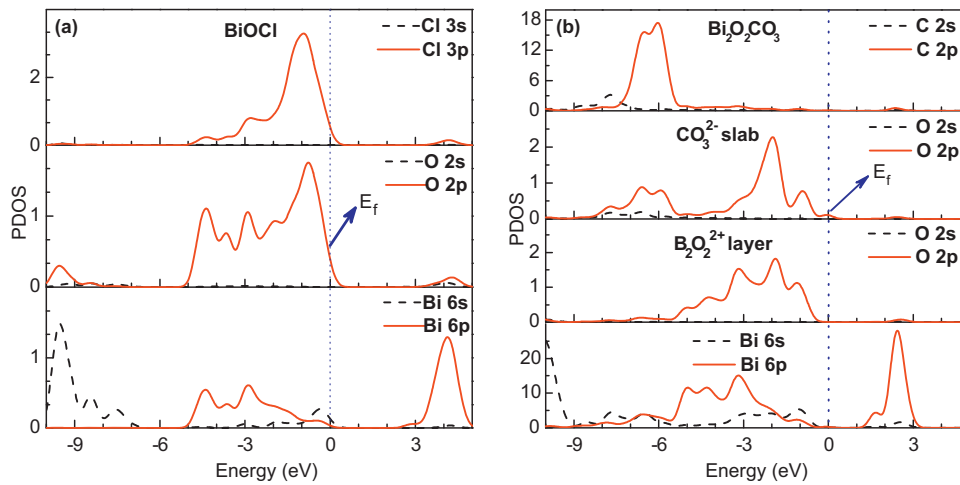


**Fig. 5.** Partial densities of states (PDOS) for tetragonal BiOCl and  $\text{Bi}_2\text{O}_2\text{CO}_3$  crystals.

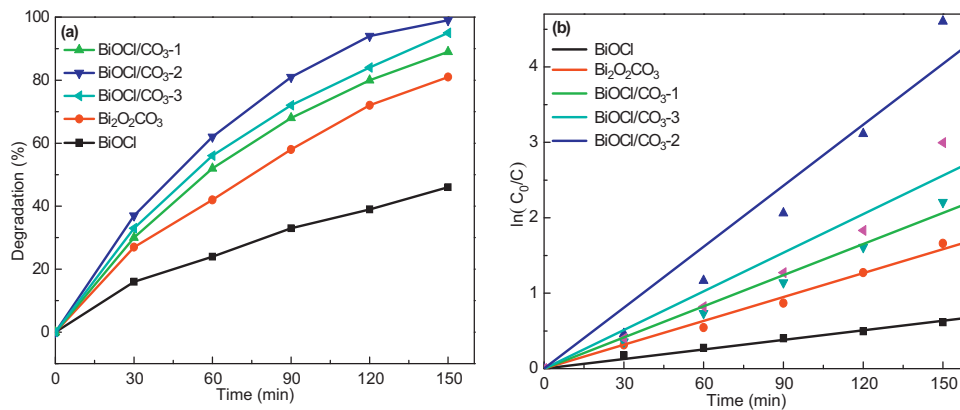


**Fig. 6.** (a) Photocatalytic degradation of MO solution over as-prepared samples as a function of irradiation time under simulated sunlight irradiation. (b) Relevant degradation rates in the presence of as-prepared samples.

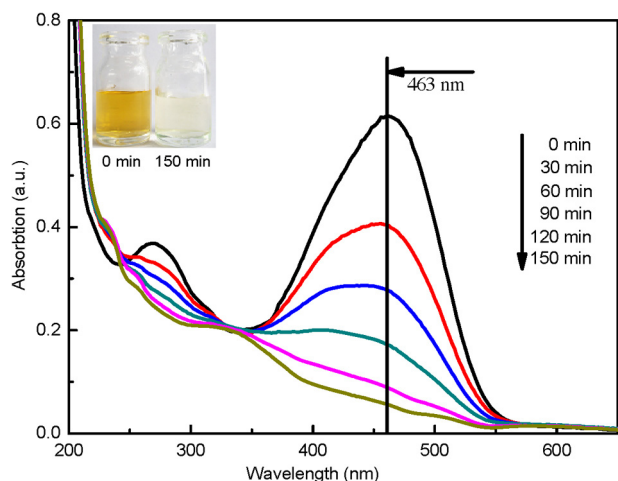


**Fig. 7.** UV-vis spectral variation of MO solution as a function of irradiation time over BiOCl/CO<sub>3</sub>-2 composite under simulated sunlight irradiation.

interfaces, which could effectively reduce the recombination probability of photo-generated electrons and holes through an internal electric field, improving the photocatalytic efficiency. The obtained subsequence of photocatalytic activity for as-prepared samples is BiOCl/CO<sub>3</sub>-2 > BiOCl/CO<sub>3</sub>-3 > BiOCl/CO<sub>3</sub>-1 > Bi<sub>2</sub>O<sub>2</sub>CO<sub>3</sub> > BiOCl, indicating that Bi<sub>2</sub>O<sub>2</sub>CO<sub>3</sub> content in the composites plays a crucial role in the photocatalytic performance, and that BiOCl/CO<sub>3</sub>-2 composite obtains the appropriate Bi<sub>2</sub>O<sub>2</sub>CO<sub>3</sub> content. Besides, excess Bi<sub>2</sub>O<sub>2</sub>CO<sub>3</sub> amounts will lead to the decrease of photocatalytic activity of as-prepared samples. It is possible that excessive Bi<sub>2</sub>O<sub>2</sub>CO<sub>3</sub> could become a recombination center and reduce the separation efficiency of photoinduced charge carriers.

Fig. 7 presents the UV-vis spectral variation of MO solution as a function of irradiation time over BiOCl/CO<sub>3</sub>-2 composite under simulated sunlight irradiation. After 150 min, the maximum absorption band of MO solution disappears completely, which indicates that MO molecules should be removed during the photocatalytic reaction process. As inset in Fig. 7, the color of supernatant changes from yellow to colorless observed by the naked eye after simulated sunlight irradiation, suggesting that BiOCl/CO<sub>3</sub>-2 composite should have an excellent photocatalytic activity. In order to further confirm whether MO is mineralized or not, the relative COD removal test of 50 mg/L MO solution over BiOCl/CO<sub>3</sub>-2 composite was carried out during the photocatalytic reaction under simulated sunlight

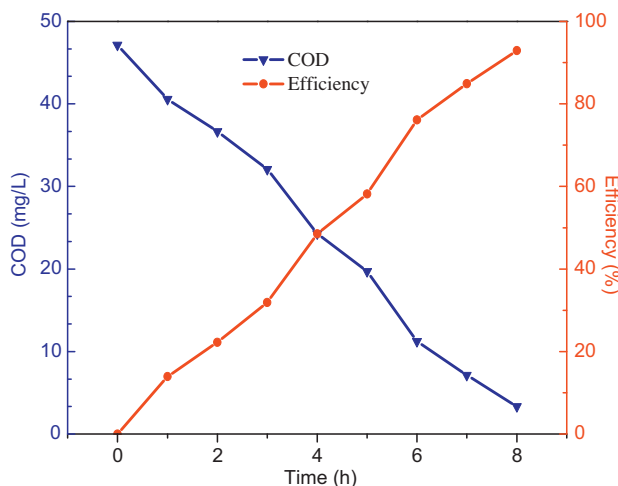


**Fig. 8.** COD removal efficiency of 50 mg/L MO solution over BiOCl/CO<sub>3</sub>-2 during the photocatalytic reaction under simulated sunlight irradiation.

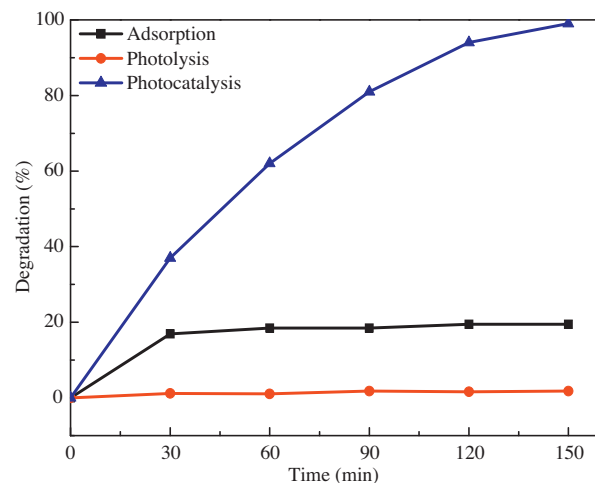


**Fig. 9.** Comparison for the effect of photolysis, adsorption, and photocatalysis on the degradation of MO.

irradiation, shown in Fig. 8. It is clearly observed that the COD removal efficiency gradually increased, and after 8 h reaction time, the COD removal efficiency achieved 95% for BiOCl/CO<sub>3</sub>-2 composite. The obtained results demonstrate that MO molecule can be more effectively mineralized by BiOCl/CO<sub>3</sub>-2 photocatalyst under simulated sunlight irradiation.

In addition, to distinguish the effect of photolysis, adsorption, and photocatalysis on the degradation rate of MO solution, the corresponding experimental processes have been performed and the obtained results are plotted in Fig. 9. The photolysis test shows that MO is very stable and hard to be decomposed under simulated sunlight irradiation without photocatalyst even after long-term, and thus, the photolysis can be ignored. After 150 min under dark condition, the adsorption efficiency of MO solution for BiOCl/Bi<sub>2</sub>O<sub>2</sub>CO<sub>3</sub> composite is only nearly 20%. However, with the presence of BiOCl/Bi<sub>2</sub>O<sub>2</sub>CO<sub>3</sub> photocatalyst, the photocatalytic degradation efficiency of MO reaches 99% under simulated sunlight irradiation. These results reveal that photocatalysis process should play an important role in the degradation of MO. The reusability and stability of BiOCl/CO<sub>3</sub>-2 have been evaluated by the recycled experiments and the results are shown in Fig. 10. For each cycle, the used catalyst was collected by centrifugation. After the second run, there was no

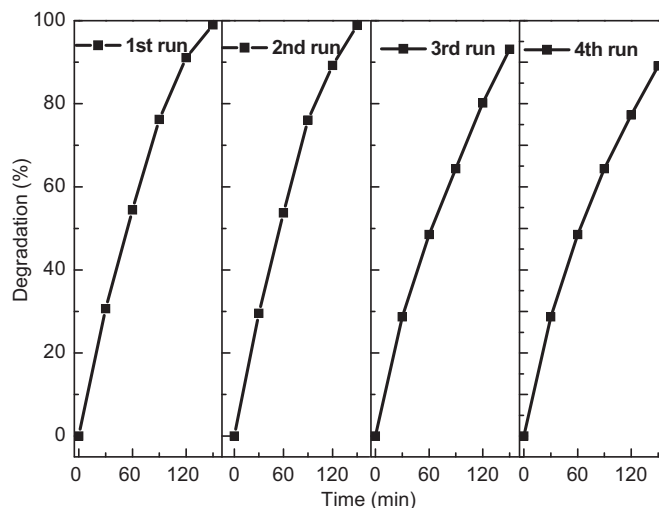


**Fig. 10.** Cycling runs in the photocatalytic degradation of MO in the presence of BiOCl/CO<sub>3</sub>-2 under simulated sunlight irradiation.

obvious loss of photocatalytic activity, and the photocatalytic efficiency of  $\text{BiOCl}/\text{CO}_3\text{-}2$  composite keeps about 90% at the fourth run. The results indicate that  $\text{BiOCl}/\text{CO}_3\text{-}2$  composite exhibits the higher stability and no photocorrosion during the photocatalytic degradation of MO. Meanwhile, the XRD patterns of  $\text{BiOCl}/\text{CO}_3\text{-}2$  composite before and after photocatalytic reaction have been characterized, and there is no detectable difference between the as-prepared and used samples (Fig. S2). Therefore, it is found that the  $\text{BiOCl}/\text{CO}_3\text{-}2$  composite has good reusability and stability.

### 3.5. Possible mechanism of activity enhancement of $\text{BiOCl}/\text{Bi}_2\text{O}_2\text{CO}_3$ composite

Based on the above discussions, single  $\text{BiOCl}$  or  $\text{Bi}_2\text{O}_2\text{CO}_3$  revealed very low photocatalytic activity under simulated sunlight irradiation, but  $\text{BiOCl}/\text{Bi}_2\text{O}_2\text{CO}_3$  composites demonstrated higher activity than individual  $\text{BiOCl}$  and  $\text{Bi}_2\text{O}_2\text{CO}_3$ . The results confirmed that the synergistic effect of  $\text{BiOCl}$  and  $\text{Bi}_2\text{O}_2\text{CO}_3$  could effectively improve the photocatalytic performance in the following several aspects: (1)  $\text{BiOCl}/\text{CO}_3\text{-}2$  composite nanosheets possess the characteristic behavior of the intersecting rows each other along the different directions and stack randomly, increasing the specific surface area and high pore volume of catalysts, facilitating the transportation of reactants and products on the photocatalyst surfaces resulting in the easy chemical reactions [25,38,39]; (2) the appropriate proportion existence of  $\text{BiOCl}$  and  $\text{Bi}_2\text{O}_2\text{CO}_3$  extends to the light response range of as-prepared samples, making full use of UV and visible light, and finally improving the quantity of photo-generated electrons and holes; (3) the relative lower crystallinity of composites could play an important factor in photocatalytic degradation due to the occurrence of impurity or defect states

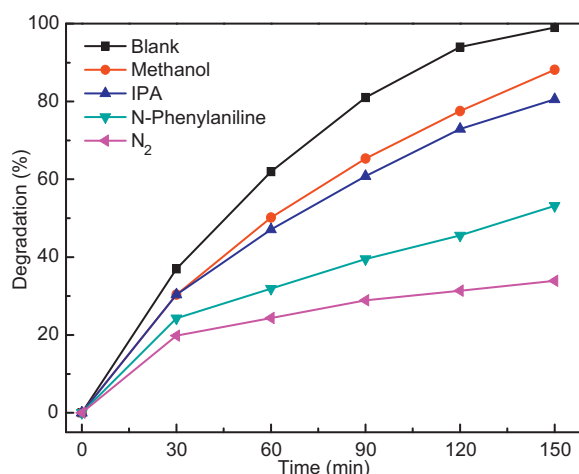
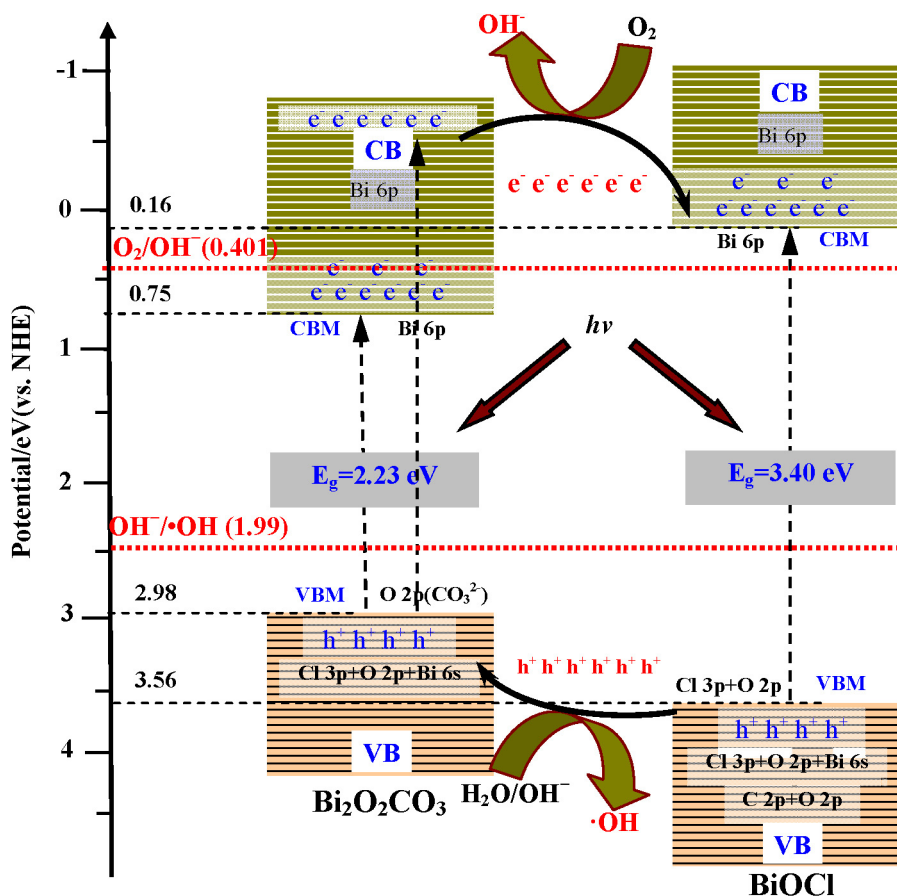


Fig. 11. Effects of methanol, *N*-phenylaniline, IPA, and  $\text{N}_2$  purging on degradation efficiency of MO over  $\text{BiOCl}/\text{CO}_3\text{-}2$ .

by a lattice distortion in the crystal transform [40]; (4) the structural and electronic properties of  $\text{BiOCl}$  and  $\text{Bi}_2\text{O}_2\text{CO}_3$  affect the effective separation of photogenerated electron-hole pairs, enhancing the photocatalytic activity of  $\text{BiOCl}/\text{Bi}_2\text{O}_2\text{CO}_3$ .

To make the reaction mechanism clear, a series of additional experiments for the effect of reactive species scavengers on the degradation of MO under simulated sunlight irradiation over  $\text{BiOCl}/\text{CO}_3\text{-}2$  have been designed and performed. The *N*-phenylaniline, methanol and 2-propanol (IPA) were adopted as electrons ( $e^-$ ), holes ( $h^+$ ) and  $\bullet\text{OH}$  scavengers in the present work,



Scheme 2. Schematic diagrams for (a) energy band of  $\text{Bi}_2\text{O}_2\text{CO}_3$  and  $\text{BiOCl}$ , (b) the formation of heterojunctions and the possible charge separation process.



respectively, and the corresponding results were shown in Fig. 11. It is found that adding the *N*-phenylaniline led to the decrease of photocatalytic degradation percentage of MO over BiOCl/CO<sub>3</sub>-2, and it is only 53% after 150 min under simulated sunlight irradiation. On the other hand, the photocatalytic degradation efficiencies of MO are 80% and 88% by the addition of IPA and methanol, respectively. In addition, the degradation percentage of MO decreased obviously via the N<sub>2</sub> purging experiment, indirectly verifying that the dissolved oxygen acted as an efficient electron trap center. The results indicated that the photo-induced electrons (e<sup>-</sup>) and holes (h<sup>+</sup>) are responsible for the enhanced photocatalytic performance of BiOCl/CO<sub>3</sub>-2.

It is generally acknowledged that the migration direction of photo-generated charge carrier is closely relative to the band edge positions of semiconductors. In order to further understand the photodegradation mechanism of MO dyes, schematic diagrams for CBM and VBM electrochemical potentials of Bi<sub>2</sub>O<sub>2</sub>CO<sub>3</sub> and BiOCl as well as the possible charge separation process of BiOCl/Bi<sub>2</sub>O<sub>2</sub>CO<sub>3</sub> composites have been designed in this work, shown in Scheme 2. It can be clearly seen that VBM potentials (3.55 and 2.98 eV vs. NHE) of BiOCl and Bi<sub>2</sub>O<sub>2</sub>CO<sub>3</sub> are more positive than the standard redox potential edge of •OH/OH<sup>-</sup> (1.99 eV vs. NHE) and •OH/H<sub>2</sub>O (2.27 eV vs. NHE), suggesting that the photo-generated holes should be more oxidative than •OH radical. In the case of Bi<sub>2</sub>O<sub>2</sub>CO<sub>3</sub>, with the longer irradiation time of simulated sunlight, the electrons in the VB of Bi<sub>2</sub>O<sub>2</sub>CO<sub>3</sub> could be activated up to the higher potential edge of CB (<-0.42 eV) [41]. Accordingly, the new CB potential of Bi<sub>2</sub>O<sub>2</sub>CO<sub>3</sub> (<-0.42 eV) is more negative than that of BiOCl (0.16 eV). As a consequence, the photo-induced electrons on the surface of Bi<sub>2</sub>O<sub>2</sub>CO<sub>3</sub> can migrate easily to the CBM of BiOCl by the interface in the composite system. Besides, the CB energy levels of BiOCl and Bi<sub>2</sub>O<sub>2</sub>CO<sub>3</sub> are mainly dominated by unoccupied Bi 6p states, and the identical energy level distribution of their CBMs exhibit the high delocalized electron states. Therefore, photo-induced electrons on the surface of Bi<sub>2</sub>O<sub>2</sub>CO<sub>3</sub> would easily transfer into the CBM of BiOCl under the inducement action of the internal electric field, leaving holes on the VB of Bi<sub>2</sub>O<sub>2</sub>CO<sub>3</sub>. Furthermore, the O 2p states of CO<sub>3</sub><sup>2-</sup> slab in Bi<sub>2</sub>O<sub>2</sub>CO<sub>3</sub> dominate the VBM of Bi<sub>2</sub>O<sub>2</sub>CO<sub>3</sub>, leading to the electronic transition from occupied O 2p states of CO<sub>3</sub><sup>2-</sup> slab in VBM to unoccupied Bi 6p states of Bi<sub>2</sub>O<sub>2</sub><sup>2+</sup> layer in CBM. On the other hand, since the VBM potential edge of Bi<sub>2</sub>O<sub>2</sub>CO<sub>3</sub> is more negative than that of BiOCl, photoinduced holes on the BiOCl surface would migrate to VBM of Bi<sub>2</sub>O<sub>2</sub>CO<sub>3</sub>. Consequently, electrons scattered in the VBM of BiOCl transfer to the surface to react with oxygen to produce OH<sup>-</sup>, and the photogenerated holes concentrated in the surface of Bi<sub>2</sub>O<sub>2</sub>CO<sub>3</sub> react with OH<sup>-</sup> and H<sub>2</sub>O to produce •OH, achieving the both an efficient consumption of holes and electrons. The photo-induced electron-hole pairs could be effectively separated at the interface of BiOCl/Bi<sub>2</sub>O<sub>2</sub>CO<sub>3</sub> and the probability of electron-hole recombination would be reduced. The analysis results are in good agreement with the above experiment phenomena of reactive species scavengers. The excellent separation of the electrons and holes undergoes reactions with the reactants adsorbed on the photocatalyst surface, and subsequently enhances the photocatalytic activity of BiOCl/Bi<sub>2</sub>O<sub>2</sub>CO<sub>3</sub> system, which will be a promising Bi-based photocatalytic composite material for degrading organic pollutants under solar light irradiation.

#### 4. Conclusions

The BiOCl, BiOCl/Bi<sub>2</sub>O<sub>2</sub>CO<sub>3</sub>, and Bi<sub>2</sub>O<sub>2</sub>CO<sub>3</sub> photocatalysts were successfully synthesized by a facile method with composition-controlled preparation technology at room temperature, in which the NaOH concentration plays a key factor for synthesizing BiOCl/Bi<sub>2</sub>O<sub>2</sub>CO<sub>3</sub> composites. The photocatalytic activities

of BiOCl/Bi<sub>2</sub>O<sub>2</sub>CO<sub>3</sub> composites for decomposing MO are obviously superior to individual BiOCl and Bi<sub>2</sub>O<sub>2</sub>CO<sub>3</sub> under simulated sunlight irradiation, and the MO degradation percentages of BiOCl/CO<sub>3</sub>-1, BiOCl/CO<sub>3</sub>-2, and BiOCl/CO<sub>3</sub>-3 composites are 90%, 99%, and 95% after 150 min, respectively, obviously higher than 46% and 81% of individual BiOCl and Bi<sub>2</sub>O<sub>2</sub>CO<sub>3</sub> photocatalyst. Besides, the relative COD removal test of 50 mg/L MO solution over BiOCl/CO<sub>3</sub>-2 composite indicates that the COD removal efficiency can achieve 95% after 8 h reaction time. The enhanced photocatalytic performance of BiOCl/Bi<sub>2</sub>O<sub>2</sub>CO<sub>3</sub> is closely related to the suitable conduction band interaction and structure characteristic, extending the optical response range and improving the efficient separation of photo-induced electron-hole pairs by the synergistic effect of BiOCl and Bi<sub>2</sub>O<sub>2</sub>CO<sub>3</sub>. In addition, based on the calculated electronic energy band structures using first-principle calculations, the CB energy levels of BiOCl and Bi<sub>2</sub>O<sub>2</sub>CO<sub>3</sub> are mainly dominated by unoccupied Bi 6p states, and exhibit the higher delocalized electron states, making photo-generated electrons on the surface of Bi<sub>2</sub>O<sub>2</sub>CO<sub>3</sub> easily transfer into CBM of BiOCl and then leaving photo-induced holes on the VB of Bi<sub>2</sub>O<sub>2</sub>CO<sub>3</sub>. Furthermore, the O 2p states of CO<sub>3</sub><sup>2-</sup> slab in Bi<sub>2</sub>O<sub>2</sub>CO<sub>3</sub> dominate the VBM of Bi<sub>2</sub>O<sub>2</sub>CO<sub>3</sub>, leading to the electronic transition from occupied O 2p states of CO<sub>3</sub><sup>2-</sup> slab in VBM to unoccupied Bi 6p states of Bi<sub>2</sub>O<sub>2</sub><sup>2+</sup> layer in CBM. Finally, the electrons scattered in the VBM of BiOCl transfer to the surface to react with oxygen to produce OH<sup>-</sup>, and the photo-generated holes concentrated in the surface of Bi<sub>2</sub>O<sub>2</sub>CO<sub>3</sub> react with OH<sup>-</sup> and H<sub>2</sub>O to produce •OH, and further oxidizing the organic pollutants. Our theoretical and experimental research results should provide the significant meaningful guidance and help for the development of potential Bi-based photocatalytic composite materials for degrading organic pollutants under solar light irradiation.

#### Acknowledgments

The authors gratefully acknowledge the financial support offered by the National Natural Science Foundation of China (No. 21176168, 21206105), International Cooperation Project of Shanxi Province (No. 2012081017), and Science and Technology Project of Taiyuan, China (No. 120123). We would express our great appreciation to Professor Peide Han for the computational guidance and help.

#### Appendix A. Supplementary data

Supplementary data associated with this article can be found, in the online version, at <http://dx.doi.org/10.1016/j.apcatb.2013.12.054>.

#### References

- [1] S. Malato, P. Fernández-Ibáñez, M.I. Maldonado, J. Blanco, W. Gernjak, *Catal. Today* 147 (2009) 1–59.
- [2] O.K. Varghese, M. Paulose, C.A. Grimes, *Nat. Nanotechnol.* 4 (2009) 592–597.
- [3] S.U.M. Khan, M. Al-Shahry, W.B. Ingler Jr., *Science* 297 (2002) 2243–2245.
- [4] N.N. Rao, V. Chaturvedi, G. Li Puma, *Chem. Eng. J.* 184 (2012) 90–97.
- [5] A. Dhakshinamoorthy, S. Navalon, A. Corma, H. García, *Energy Environ. Sci.* 5 (2012) 9217–9233.
- [6] K.L. Zhang, C.M. Liu, F.Q. Huang, C. Zheng, W.D. Wang, *Appl. Catal. B: Environ.* 68 (2006) 125–129.
- [7] Z.H. Ai, W.K. Ho, S.C. Lee, L.Z. Zhang, *Environ. Sci. Technol.* 43 (2009) 4143–4150.
- [8] B. Sarwan, B. Pare, A.D. Acharya, S.B. Jonnalagadda, *J. Photochem. Photobiol. B: Biol.* 116 (2012) 48–55.
- [9] Y. Tian, C.F. Guo, Y.J. Guo, Q. Wang, Q. Liu, *Appl. Surf. Sci.* 258 (2012) 1949–1954.
- [10] J. Jiang, K. Zhao, X.Y. Xiao, L.Z. Zhang, *J. Am. Chem. Soc.* 134 (2012) 4473–4476.
- [11] J.Y. Xiong, G. Cheng, F. Qin, R.M. Wang, H.Z. Sun, R. Chen, *Chem. Eng. J.* 220 (2013) 228–236.
- [12] X.C. Zhang, X.X. Liu, C.M. Fan, Y.W. Wang, Y.F. Wang, Z.H. Liang, *Appl. Catal. B: Environ.* 132–133 (2013) 332–341.
- [13] C.F. Guo, J.M. Zhang, Y. Tian, Q. Liu, *J. Am. Chem. Soc.* 133 (2011) 8211–8215.

- [14] S. Shamaila, A.K.L. Sajjad, F. Chen, J.L. Zhang, *J. Colloid Interf. Sci.* 356 (2011) 465–472.
- [15] X.F. Chang, G. Yu, J. Huang, Z. Li, S.F. Zhu, P.F. Yu, C. Cheng, S.B. Deng, G.B. Ji, *Catal. Today* 153 (2010) 193–199.
- [16] K. Yang, C.L. Yu, L.N. Zhang, J.M. Yu, *J. Synth. Cryst.* 41 (2012) 171–176.
- [17] H.F. Cheng, B.B. Huang, X.Y. Qin, X.Y. Zhang, Y. Dai, *Chem. Commun.* 48 (2012) 97–99.
- [18] B.C. Cao, P.Y. Dong, S. Cao, Y.H. Wang, *J. Am. Ceram. Soc.* 96 (2013) 544–548.
- [19] X.Y. Chen, Z.J. Zhang, S.W. Lee, *J. Solid State Chem.* 181 (2008) 166–174.
- [20] L. Huang, L.P. Li, T.J. Yan, G.S. Li, *Chin. J. Struct. Chem.* 28 (2009) 1458–1464.
- [21] C.F. Guo, J.M. Zhang, Y. Tian, Q. Liu, *ACS Nano* 6 (2012) 8746–8752.
- [22] F. Dong, W.K. Ho, S.C. Lee, Z.B. Wu, M. Fu, S.C.Z.Y. Huang, *J. Mater. Chem.* 21 (2011) 2428–2436.
- [23] L. Chen, R. Huang, S.F. Yin, S.L. Luo, C.T. Au, *Chem. Eng. J.* 193–194 (2012) 123–130.
- [24] Y. Zheng, F. Duan, M.Q. Chen, Y. Xie, *J. Mol. Catal. A: Chem.* 317 (2010) 34–40.
- [25] T.Y. Zhao, J.T. Zai, M. Xu, Q. Zou, Y.Z. Su, K.X. Wang, X.F. Qian, *CrystEngComm* 13 (2011) 4010–4017.
- [26] H.F. Cheng, B.B. Huang, K.S. Yang, Z.Y. Wang, X.Y. Qin, X.Y. Zhang, Y. Dai, *ChemPhysChem* 11 (2010) 2167–2173.
- [27] F. Dong, Y.J. Sun, M. Fu, W.K. Ho, S.C. Lee, Z.B. Wu, *Langmuir* 28 (2012) 766–773.
- [28] M.D. Segall, P.L.D. Lindan, M.J. Probert, P.J. Hasnip, S.J. Clark, M.C. Payne, *J. Phys. Condens. Matter* 14 (2002) 2717–2744.
- [29] J.P. Perdew, K. Burke, M. Ernzerhof, *Phys. Rev. Lett.* 77 (1996) 3865–3868.
- [30] H.J. Monkhorst, J.D. Pack, *Phys. Rev. B* 13 (1976) 5188–5192.
- [31] J.C. Wang, P. Liu, X.Z. Fu, Z.H. Li, W. Han, X.X. Wang, *Langmuir* 25 (2009) 1218–1223.
- [32] P. Madhusudan, J.R. Ran, J. Zhang, G. Yu, J.G. Liu, *Appl. Catal. B: Environ.* 110 (2011) 286–295.
- [33] L. Liu, J. Jiang, S.M. Jin, Z.M. Xia, M.T. Tang, *CrystEngComm* 13 (2011) 2529–2532.
- [34] J.Y. Xia, L. Liu, S.M. Jin, Z.M. Xia, M.T. Tang, *Procedia Eng.* 27 (2012) 1441–1447.
- [35] A.H. Nethercot Jr., *Phys. Rev. Lett.* 33 (1974) 1088–1091.
- [36] W.L. Huang, Q.S. Zhu, *J. Comput. Chem.* 30 (2009) 1882–1891.
- [37] X.C. Zhang, L.J. Zhao, C.M. Fan, Z.H. Liang, P.D. Han, *Comput. Mater. Sci.* 61 (2012) 180–184.
- [38] Y.D. Hou, X.C. Wang, L. Wu, X.F. Chen, Z.X. Ding, X.X. Wang, X.Z. Fu, *Chemosphere* 72 (2008) 414–421.
- [39] X.L. Hu, G.S. Li, J.C. Yu, *Langmuir* 26 (2010) 3031–3039.
- [40] M. Wuttig, D. Lüsebrink, D. Wamwangi, W. Wenig, M. Gilleßen, R. Dronskowski, *Nat. Mater.* 6 (2007) 122–128.
- [41] W.J. Wang, H.F. Cheng, B.B. Huang, X.J. Lin, X.Y. Qin, X.Y. Zhang, Y. Dai, *J. Colloid Interf. Sci.* 402 (2013) 34–39.